



Design and synthesis of core-shell structured *meso*-Cu-SSZ-13@mesoporous aluminosilicate catalyst for SCR of NO_x with NH₃: Enhancement of activity, hydrothermal stability and propene poisoning resistance

Tao Zhang, Feng Qiu, Junhua Li*

State Key Joint Laboratory of Environment Simulation and Pollution Control, School of Environment, Tsinghua University, Beijing, 100084, China

ARTICLE INFO

Article history:

Received 25 January 2016
Received in revised form 26 April 2016
Accepted 30 April 2016
Available online 4 May 2016

Keywords:

NH₃-SCR
meso-Cu-SSZ-13@MAS
Activity
Hydrothermal stability
Propene poisoning resistance

ABSTRACT

A core-shell structured composite material with a mesoporous aluminosilicate (MAS) shell and mesopore-containing SSZ-13 (*meso*-SSZ-13) core was first synthesized by combining controlled desilication with subsequent self-assembly. The corresponding catalyst was subsequently prepared by a copper ion-exchange method. This catalyst can simultaneously solve three major problems existing in the previous Cu-SSZ-13 catalyst for NO_x emission control from diesel engine exhaust, i.e., low temperature activity, hydrothermal stability and propene poisoning resistance. In comparison with Cu-SSZ-13, the *meso*-Cu-SSZ-13@mesoporous aluminosilicate (*meso*-Cu-SSZ-13@MAS) catalyst showed higher SCR activity across the entire temperature range. This increase was observed due to increasing the amount of active Cu species (isolated Cu²⁺ ions) and fewer pore diffusion limitations. The MAS shell with a “concrete with crushed stone”-like mesostructure could prevent the dealumination of *meso*-SSZ-13 core effectively, and therefore enhanced the hydrothermal stability of the *meso*-Cu-SSZ-13@MAS catalyst. Additionally, *meso*-Cu-SSZ-13@MAS exhibited higher hydrocarbon poisoning resistance because its external surface has fewer active sites for propene oxidation reaction.

© 2016 Elsevier B.V. All rights reserved.

1. Introduction

Currently, the selective catalytic reduction of NO_x with NH₃ (NH₃-SCR) is one of the most promising technologies for control of NO_x emissions control from diesel engine exhaust. The core part of SCR technology is the catalyst. Many different catalysts have been studied for NH₃-SCR reaction. Among these catalysts, transition metal-exchanged (e.g., containing Cu, Fe) zeolite catalysts have been studied intensively for meeting diesel NO_x emission standards [1]. In recent years, small pore Cu-exchanged zeolite catalysts, such as Cu-SSZ-13 and Cu-SAPO-34, have received great attention due to their outstanding activity and hydrothermal durability [2–4]. Cu-SSZ-13 shows improved activity, N₂ selectivity, and hydrothermal stability compared to Cu-ZSM-5, Cu-Y and Cu-beta [5]. The synthesis method of SSZ-13 zeolite was first reported by Zones in 1985 [6]. However, the very costly structure-directing agent N,N,N-trimethyl-1-adamantammonium hydroxide (TMAdaOH) limits the

wide application of this material as a catalyst support. More recently, Chen et al. proposed an economical way for SSZ-13 preparation with the essentially cheap choline chloride as a template [7]. Furthermore, Ren et al. designed a one-pot synthesis method for the Cu-SSZ-13 catalyst using low-cost copper-tetraethylenepentamine (Cu-TEPA) as a novel template. Xie et al. improved on this preparation method by post-treatment [8]. Corma et al. proposed that Cu-TEPA could also be used as a co-SDA, together with TMAdaOH, to allow Si/Al ratios and Cu contents to be readily controlled [9].

There are several extensive studies of the Cu-SSZ-13 catalyst, exploring such facets as active species [10–14], reaction mechanism [15–18], reaction kinetics [19,20], hydrothermal stability [5,21–23], and poisoning mechanism [24–27]. However, there are still three major problems obstructing the practical use of this zeolite catalyst in NO_x removal from diesel emissions. Firstly, the “light-off” temperature for the Cu-SSZ-13 catalyst prepared by the conventional ion-exchange method is close to 200 °C [28]. Nevertheless, for future applications, the new internal combustion engine (ICE) operation modes lead to much lower exhaust temperatures than those of current engines. The steady-state operation of the NO_x reduction technology at 150 °C may be required [29]. Sec-

* Corresponding author.

E-mail address: lijunhua@tsinghua.edu.cn (J. Li).

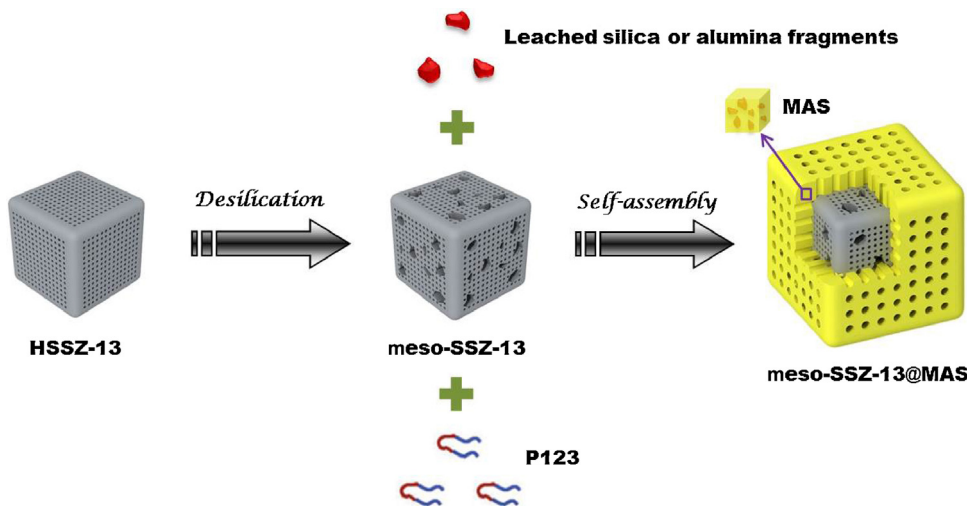


Fig. 1. Schematic representation of the preparation of meso-SSZ-13@MAS composite.

ondly, for the Cu-SSZ-13 catalyst, hydrothermal aging still results in remarkably lower NO_x conversions at all temperatures tested [22]. Cu migration, acidity loss, and dealumination are primarily responsible for the hydrothermal aging of Cu-SSZ-13 catalysts [21]. In practical application, high hydrothermal durability is required for the SCR catalyst to remain effective for NO_x emission control because the collected soot is frequently removed from the DPF at high temperatures (650°C), [30]. Therefore, it is necessary to improve the hydrothermal stability of the Cu-SSZ-13 catalyst. Finally, the catalytic performance of the Cu-SSZ-13 catalyst is inhibited in the presence of propene. The main reason for the decrease of NH_3 -SCR activity is coke deposition on the active sites [24,25]. Moreover, coke formation is the primary factor affecting the pore structure and acidity of the zeolite [24].

Few studies address the problems listed above. In the present work, a core-shell structured catalyst, composed of an ordered mesoporous aluminosilicate (MAS) shell and a mesopore-containing Cu-SSZ-13 (*meso*-Cu-SSZ-13) core, was prepared for the first time. This material contains interconnected hierarchical pores and can simultaneously solve the above three problems existing in the previous Cu-SSZ-13 catalyst. Note that the reasons for the use of MAS shell instead of pure silicate one are the following: (1) the MAS shell was prepared using the silica or alumina species leached from the SSZ-13 by alkaline treatment and without additional silica source. However, the preparation of pure silicate shell needs to add additional silica source; (2) the mesoporous structure into SSZ-13 molecular sieve was introduced to reduce intra-crystalline (pore) diffusion limitations existing in it. This can be simultaneously achieved while preparing the MAS shell. In contrast, only the preparation of pure silicate shell could not achieve the above aim. Further, various techniques (XRD, SEM, TEM, N_2 adsorption-desorption, ICP-AES, NMR, TGA, H_2 -TPR, EPR, NH_3 -TPD, and *in-situ* DRIFTS), as well as SCR activity measurements, were used to understand the relationship between structure and superior performance of the core-shell structured catalyst.

2. Experimental

2.1. Preparation of the supports

A schematic representation of the process for the preparation of core-shell structured meso-SSZ-13@mesoporous aluminosilicate (denoted as meso-SSZ-13@MAS) material is shown in Fig. 1. The typical preparation procedure of the meso-SSZ-13@MAS material

is as follows. 1 g HSSZ-13 zeolite (provided by Zeolite company, Si/Al = 11.2) was desilicated in 100 mL NaOH solution (0.1 mol/L) at 75°C for 2 h. At this moment, the mesoporous SSZ-13 (denoted as meso-SSZ-13) can be obtained. Next, 100 mL deionized water and 96 mL ethanol containing 2.0 g P123 were added into the above suspension. Then, 0.1 mol/L HCl solution was added into the mixture to adjust its pH value to *ca.* 5, with the aim of well matching the iso-electric point between mesoporous SSZ-13 and the silica gel. The mixture was ultrasonicated for 1 h to form a uniform suspension. After reaction at 35°C for 48 h, the mixture was further heated at 70°C for 24 h. In this process, the leached silica and alumina species were self-assembled on the surface of mesoporous SSZ-13 to form core-shell structured material. Finally, the product was washed with deionized water and ethanol in turn for three times, dried in air at 100°C overnight, and calcined at 550°C for 6 h.

For comparison, other samples (meso-SSZ-13 and MAS) were prepared. The meso-SSZ-13 sample was obtained by desilication only. The MAS sample, namely mesoporous silica containing Al, was prepared by the same procedures mentioned above, but using only the filtrate after removing undissolved bulky SSZ-13 particles by vacuum filtration.

2.2. Preparation of the catalysts

The catalysts were prepared by conventional aqueous solution ion-exchange method. First, the corresponding support was ion-exchanged using excess amount of 0.1 mol/L NH_4NO_3 at 80°C for 12 h to obtain its NH_4^+ form. Then, the solid was filtered and dried at 100°C for 12 h before repeating the above process two times. Cu ion exchange was performed by mixing the NH_4^+ support with a $\text{Cu}(\text{CH}_3\text{COO})_2$ solution (SSZ-13, meso-SSZ-13@MAS and MAS: 0.01 mol/L; meso-SSZ-13: 0.0075 mol/L) at room temperature (RT) for 12 h. Next, the powder was filtered and thoroughly washed with distilled water. This was followed by drying at 100°C for 12 h and calcining at 550°C in air for 6 h.

The hydrothermal aging of the catalyst was performed in a flowing wet air containing 10% H_2O and held at 750°C for 16 h.

2.3. Characterization of the supports and the catalysts

X-ray diffraction (XRD) patterns were taken on a Rigaku D/max-2200 Diffractometer equipped with a $\text{Cu K}\alpha$ detector. The N_2 adsorption and desorption measurements were performed at 77 K using a Quantachrome Autosorb-6 analyzer. The sam-

oles were degassed at 300 °C for 4 h before the measurement. The elemental compositions of the catalysts were analyzed by inductive coupled plasma atomic emission spectrometry (ICP-AES) (PE, OPTIMA5300DV). Scanning electron microscopy (SEM) measurements were carried out on a Quanta 200F instrument with accelerating voltage of 5 kV. Transmission electron microscope (TEM) images were obtained using a JEOL JEM 2100 electron microscope equipped with a field emission source at an accelerating voltage of 200 kV. The elemental local and mapping analyses were acquired by energy-dispersive spectroscopy (EDS) using a Tecnai F20 electron microscope equipped with a STEM unit and a CCD detector. Nuclear magnetic resonance (NMR) spectra were acquired on a Bruker AVANCE III 400 MHz instrument. For ²⁹Si NMR measurement, the spectra were obtained at a spinning speed of 5 kHz at 79.302 MHz. For ²⁷Al NMR measurement, the spectra were recorded with a spinning rate of 12 kHz at 104.012 MHz. ²⁹Si and ²⁷Al chemical shifts were referenced to tetramethylsilane and 1 M aqueous Al(NO₃)₃ solution, respectively. Electron paramagnetic resonance (EPR) experiments were conducted on a JEOL X-band spectrometer equipped with a liquid nitrogen cryostat. Temperature programmed reduction with H₂ (H₂-TPR) experiments were carried out on a ChemiSorb2720 TPX chemisorption analyzer. The samples were pretreated at 300 °C in Ar for 1 h and cooled to ambient temperature. Then, H₂-TPR was performed from ambient to 1000 °C with a heating rate of 10 °C min⁻¹ under 10% H₂/Ar gas flow of 50 mL min⁻¹. Temperature programmed desorption (TPD) of NH₃ was carried out using a MultiGas 2030HS FTIR spectrometer. Initially, all the samples were heated to 500 °C in N₂ flow (200 mL min⁻¹) and maintained at 500 °C for 1 h. The NH₃ adsorption was performed at 100 °C. After saturation, the samples were purged with N₂ at the same temperature for 2 h. Then, the desorption of NH₃ was performed in the range of 100–700 °C at a ramp of 10 °C min⁻¹. In situ DRIFTS experiments were performed using a Nicolet NEXUS 6700 FTIR spectrometer equipped with a high temperature reaction chamber. The pretreatment was conducted at 500 °C in N₂ for 1 h. The DRIFTS spectra were recorded in the range of 4000–650 cm⁻¹ by accumulating 32 scans with a resolution of 4 cm⁻¹.

2.4. Catalyst evaluation

The SCR reaction tests were performed by loading 0.02 g catalysts of 40–60 mesh in the micro-scale reactor. The typical composition of inlet gas was 500 ppm NO, 500 ppm NH₃, 500 ppm C₃H₆ (when used), 5% O₂, and 5% H₂O with a balance of N₂. The total flow rate was 200 mL min⁻¹ and the corresponding gas hourly space velocity (GHSV) was 400,000 h⁻¹. The outlet gas concentration was monitored by a MultiGas 2030HS FTIR spectrometer. The NO_x conversion, N₂ selectivity and reaction rate (r) were calculated using the equations:

$$\text{NO}_x \text{Conversion} = \frac{[\text{NO} + \text{NO}_2]_{\text{inlet}} - [\text{NO} + \text{NO}_2 + \text{N}_2\text{O}]_{\text{outlet}}}{[\text{NO} + \text{NO}_2]_{\text{inlet}}} \times 100\% \quad (1)$$

$$\text{N}_2 \text{Selectivity} = \left(1 - \frac{2[\text{N}_2\text{O}]_{\text{outlet}}}{[\text{NO}_x]_{\text{inlet}} + [\text{NH}_3]_{\text{inlet}} - [\text{NO}_x]_{\text{outlet}} - [\text{NH}_3]_{\text{outlet}}} \right) \times 100\% \quad (2)$$

$$r = \frac{F}{W}(-\ln(1-x)) \quad (3)$$

where F is the NO feeding rate (moles of NO per s), W is the weight of the catalyst (g) and x the relative NO conversion.

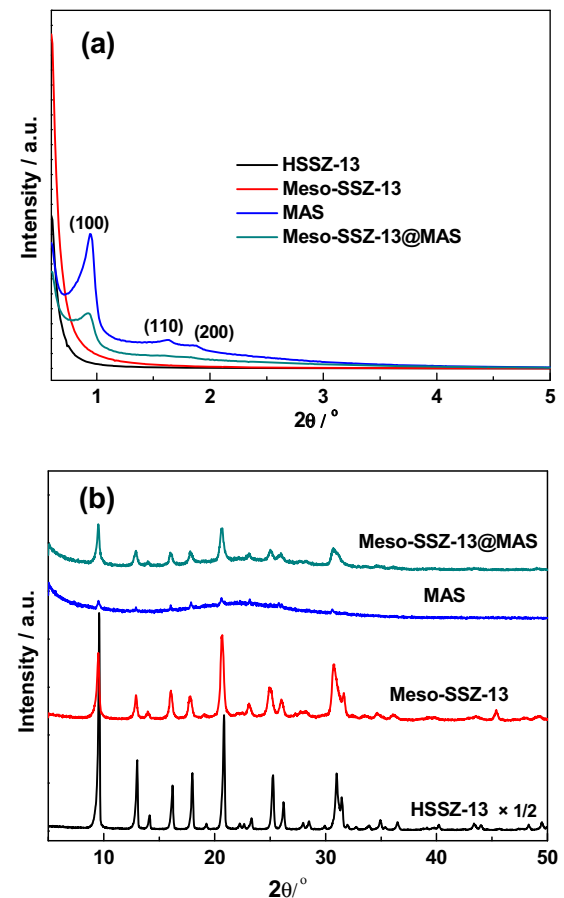


Fig. 2. XRD patterns of the as-synthesized materials in the small-angle domain (a) and in the wide-angle domain (b).

3. Results

3.1. Support characterization

Fig. 2 shows the XRD patterns of the as-synthesized materials. As shown in Fig. 2a, MAS exhibited three well-resolved diffraction peaks indexed as (100), (110), and (200) reflections, which are consistent with the SBA-15 structure. This finding indicates that the as-synthesized MAS possesses highly ordered hexagonal (space group *p6 mm*) symmetry and a well-ordered mesoporous structure [31]. By contrast, the intensities of the peaks belonging to *meso*-SSZ-13@MAS were weaker than those of MAS, which may be due to the presence of the SSZ-13 phase in the composite. However, the HSSZ-13 and *meso*-SSZ-13 samples did not exhibit any diffraction peaks in the small-angle domain. As shown in Fig. 2b, HSSZ-13, *meso*-SSZ-13, and *meso*-SSZ-13@MAS show the typical XRD patterns of zeolites with the CHA framework topology [32], confirming that the CHA structure was maintained after treatment with alkaline solution. Notably, the crystallinity of *meso*-SSZ-13, as observed by XRD, showed a dramatic decrease from that of HSSZ-13. This finding means that desilication has a considerable influence on the long-range ordering of the zeolite. In contrast with *meso*-SSZ-13, the weakening of the CHA structure-related diffractions for *meso*-SSZ-13@MAS is simply because of a diluting effect of the mesophase shell on the crystalline component *meso*-SSZ-13 in the composite. In addition, it is important to note that MAS still exhibited characteristic diffraction peaks due to the CHA topology, although they were weak in intensity.

The N₂ adsorption-desorption isotherms of the supports are shown in Fig. 3a. The pristine HSSZ-13 sample showed a type

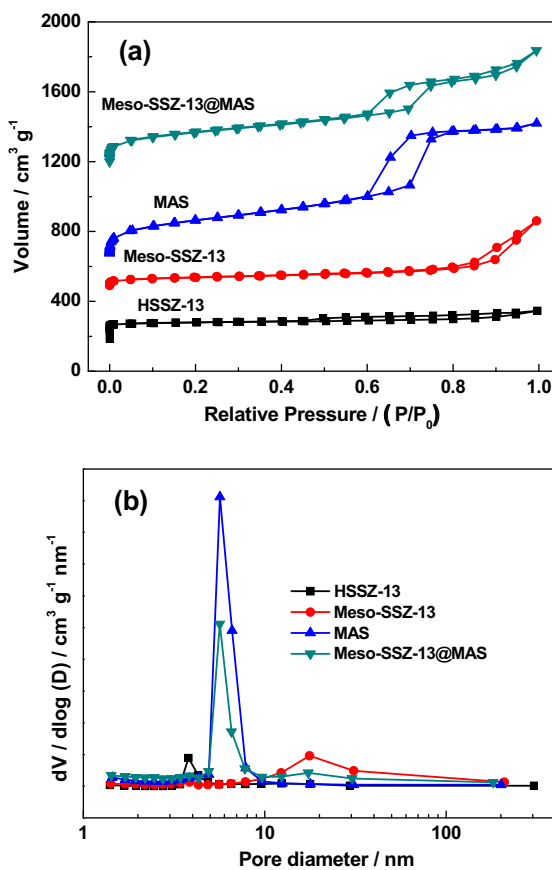


Fig. 3. N_2 adsorption-desorption isotherms (a) and pore size distribution (b) of the as-synthesized materials.

I isotherm, characteristic of microporous materials, whereas the isotherms of *meso*-SSZ-13 showed a H4-type hysteresis loop. This finding indicates that a hierarchical porous system including both micropores and mesopores, is formed during desilication by NaOH. The MAS and *meso*-SSZ-13@MAS samples exhibited an uptake at low P/P_0 , similar to the HSSZ-13 sample. These isotherms are typical type-IV isotherms with a H1-type hysteresis loop and a sharp capillary condensation step in the P/P_0 range of 0.6–0.8. The textual and structural properties of the supports are shown in Table 1. Contrary to reports on topologies other than CHA, the desilication process was accompanied by a decrease in BET surface area (S_{BET}) [33,34]. Meanwhile, the micropore volume (V_{mic}) decreased grad-

ually from 0.23 to 0.13 cm^3/g , whereas the total pore volume (V_t) increased from 0.34 to 0.68 cm^3/g . On the other hand, the external surface area (S_{ext}) increased significantly due to mesopore formation. After coating with a MAS shell, the S_{BET} , S_{ext} , and V_t of the *meso*-SSZ-13@MAS sample further increased in comparison with the HSSZ-13 and *meso*-SSZ-13 samples. The pore size distribution (PSD) derived from the desorption branches of the samples illustrates the existence of uniform mesopores ~ 5.7 nm in MAS and *meso*-SSZ-13@MAS (Fig. 3b and Table 1). Additionally, the peaks located from 10 to 30 nm were observed for *meso*-SSZ-13 and *meso*-SSZ-13@MAS.

The morphology of the supports was investigated by means of SEM and TEM. The pristine HSSZ-13 sample exhibited typical cubic crystals with different sizes (Fig. 4a₁ and b₁). When HSSZ-13 was treated with NaOH, a number of small-diameter cavities and slits were clearly perceived at the surface of the particles (Fig. 4a₂). This finding indicates that mesopores were introduced into the crystals of *meso*-SSZ-13, which can be further inferred from the black areas with a distribution of white dots in the TEM image (Fig. 4b₂). Fig. 4c₁ shows that MAS has an amorphous bulk morphology, consisting of agglomerates of countless small particles. The TEM image in Fig. 4c₂ verifies that the MAS sample had 2D p6 mm hexagonal structures, which is consistent with the previous XRD results. In the core-shell structured *meso*-SSZ-13@MAS, there was a new phase (i.e., MAS) visibly grown on the surface of the *meso*-SSZ-13 crystals (Fig. 4d₁). Consistent with the SEM image, the TEM images showed that the *meso*-SSZ-13 crystal is enclosed by a MAS shell (Fig. 4d₁ and S1), which results in the worm-like appearance of the mesoporous structure. This phase transition for MAS (from a hexagonal to a worm-like structure) is because of the difficulty of coating a two-dimensional structure with hexagonal symmetry on the irregular surface of the *meso*-SSZ-13 crystals. However, the worm-like mesoporous structure may allow greater interconnectivity between the mesopores in the shell and the mesopores in the shell more chances to interconnect with the micropores inside the *meso*-SSZ-13 core, in comparison with ordered hexagonal channels.

3.2. NH_3 -SCR activity and kinetics over the fresh catalysts

Fig. 5 shows NO_x conversions as a function of reaction temperature between 100 and 550 °C, over the Cu-SSZ-13, *meso*-Cu-SSZ-13, *meso*-Cu-SSZ-13@MAS and Cu-MAS catalysts studied. For comparison, the catalytic activity of HSSZ-13 is also shown in Fig. 5. At low temperatures below 175 °C, the results clearly demonstrate that the NH_3 -SCR reaction was essentially only carried out on Cu sites, while the zeolite carrier itself did not directly

Table 1

Textural properties of the supports and the corresponding catalysts before and after hydrothermal aging.

| Samples | S_{BET}^b ($\text{m}^2 \text{ g}^{-1}$) | S_{ext}^c ($\text{m}^2 \text{ g}^{-1}$) | V_t^d ($\text{cm}^3 \text{ g}^{-1}$) | V_{mes}^e ($\text{cm}^3 \text{ g}^{-1}$) | V_{mic}^f ($\text{cm}^3 \text{ g}^{-1}$) | d_{BJH}^f (nm) | Si/Al ^g | Cu content ^g (wt.%) |
|---|--|--|--|---|---|-------------------------|--------------------|--------------------------------|
| HSSZ-13 | 558.1 | 50.7 | 0.34 | 0.14 | 0.23 | – | 11.2 | – |
| <i>meso</i> -SSZ-13 | 512.6 | 118.7 | 0.68 | 0.57 | 0.13 | 17.7 | 4.3 | – |
| MAS | 729.4 | 693.4 | 1.17 | 1.22 | <0.01 | 5.7 | 80.8 | – |
| <i>meso</i> -SSZ-13@MAS | 628.0 | 458.0 | 1.06 | 0.99 | 0.14 | 5.7 | 11.0 | – |
| Cu-SSZ-13-F ^a | 516.6 | 41.6 | 0.33 | 0.13 | 0.22 | – | 11.1 | 2.41 |
| <i>meso</i> -Cu-SSZ-13-F ^a | 468.3 | 103.3 | 0.60 | 0.50 | 0.11 | 17.7 | 4.4 | 2.46 |
| <i>meso</i> -Cu-SSZ-13@MAS-F ^a | 568.5 | 381.8 | 0.83 | 0.78 | 0.13 | 5.6 | 11.1 | 2.43 |
| Cu-SSZ-13-A ^a | 462.3 | 24.4 | 0.25 | 0.13 | 0.14 | – | 11.1 | 2.41 |
| <i>meso</i> -Cu-SSZ-13-A ^a | 130.1 | 62.4 | 0.42 | 0.40 | 0.03 | 12.5 | 4.4 | 2.46 |
| <i>meso</i> -Cu-SSZ-13@MAS-A ^a | 517.1 | 332.5 | 0.73 | 0.71 | 0.11 | 5.6 | 11.1 | 2.43 |

^a F and A represent fresh and aged samples, respectively.

^b Calculated by the BET method.

^c Calculated using the t-plot method.

^d The total pore volume was obtained at a relative pressure of 0.99.

^e Calculated using the BJH method.

^f Mesopore diameter was calculated using the BJH method.

^g Determined by ICP-AES.

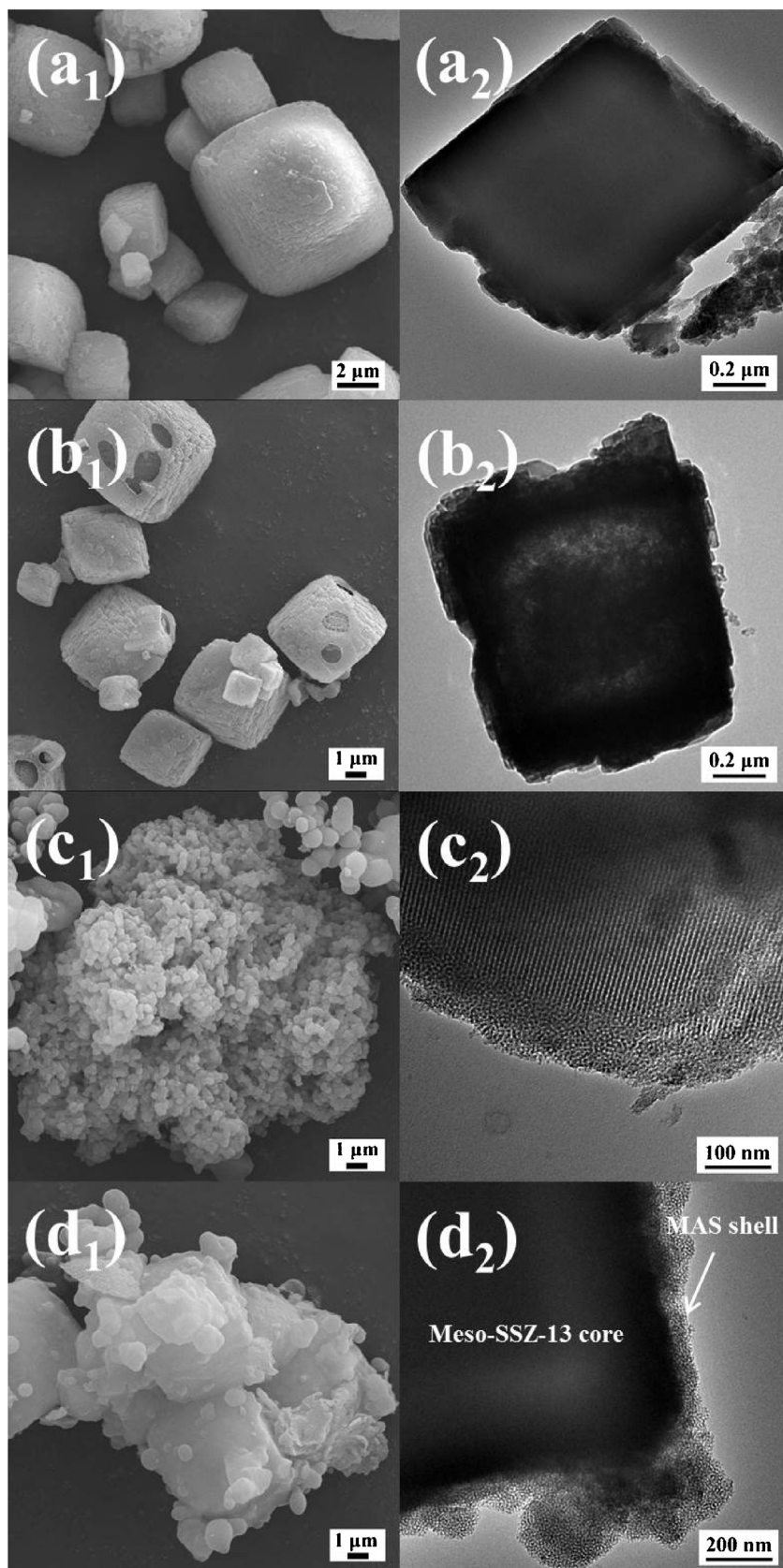


Fig. 4. SEM and TEM images of HSSZ-13 (a₁ and a₂), meso-SSZ-13 (b₁ and b₂), MAS (c₁ and c₂) and meso-SSZ-13@MAS (d₁ and d₂).

contribute to the activity. At temperatures below 250 °C, NO_x conversions over Cu-SSZ-13 sample were lower than those over meso-Cu-SSZ-13 and meso-Cu-SSZ-13@MAS samples. Furthermore,

the latter two samples showed higher NO_x conversions in comparison with Cu-SSZ-13 above 350 °C. The order of activity of these catalysts in the entire temperature region is as follows:

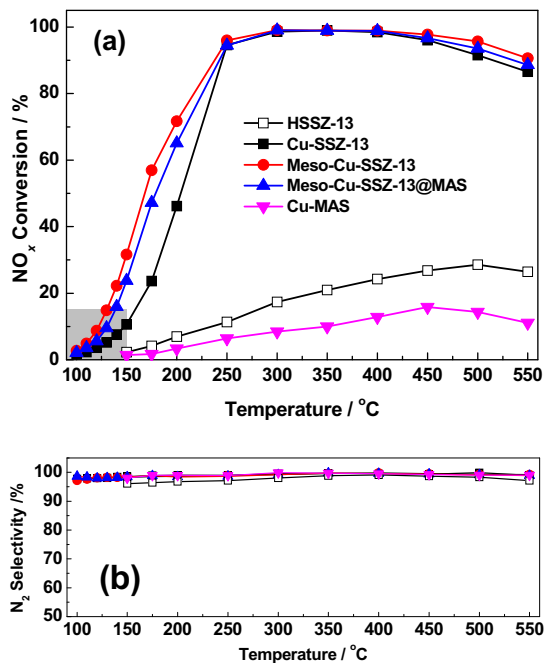


Fig. 5. NO_x conversion and N₂ selectivity as a function of temperature in the NH₃-SCR reaction over HSSZ-13, Cu-SSZ-13, meso-Cu-SSZ-13, meso-Cu-SSZ-13@MAS, and Cu-MAS catalysts. Reaction conditions: [NO] = [NH₃] = 500 ppm, [O₂] = 5%, [H₂O] = 5%, N₂ balance, total flow rate 200 mL min⁻¹ and GHSV = 400,000 h⁻¹.

meso-Cu-SSZ-13 > meso-Cu-SSZ-13@MAS > Cu-SSZ-13. In addition, compared with meso-Cu-SSZ-13@MAS, Cu-MAS exhibited poor NO_x conversions. This suggests that NH₃-SCR reaction mainly occurred on the meso-Cu-SSZ-13 core, while the MAS shell contributed little to the activity.

Recently, Gao et al. have found that intra-crystalline (pore) diffusion limitations play a significant role in the low-temperature kinetics of the Cu-SSZ-13 catalyst [19]. Thus, NH₃-SCR kinetics were also measured over our catalysts with different morphologies. It is worth noting that a GHSV of 400,000 h⁻¹ allows us to rule out interparticle mass transfer limitations [20]. Fig. S2a displays the normalized SCR rates using the Eq. (3) shown above. The reaction rates for all the samples increased with increasing temperature below 300 °C. Then, turnover frequencies (TOFs, which are defined as the moles of NO molecules converted per second by the moles of Cu atoms in the catalysts) within the differential regime were calculated. And, the results are displayed in Fig. S2b in the form of Arrhenius plots where the reaction rates are normalized as TOFs. Besides, the preexponential factors (in ln(A)) and the apparent reaction activation (E_a) values are also displayed. Interestingly, all three samples displayed rather different lnA and E_a values. Among them, meso-Cu-SSZ-13 displayed the highest E_a value (72 kJ/mol), indicating that it has the fewest pore diffusion limitations [35]. The likely origin for this phenomenon will be discussed in more detail below.

3.3. Hydrothermal stability

In order to probe hydrothermal stability, and to investigate the effects of hydrothermal aging on the catalytic activities and the catalyst structures, the above three catalysts were further treated in air with 10% H₂O at 750 °C for 16 h. The NH₃-SCR performance of the aged catalysts is shown in Fig. S3. Additionally, on the base of the results shown in Fig. 5, the aged Cu-SSZ-13 and the meso-Cu-SSZ-13 catalysts lost their NH₃-SCR activity significantly, while the meso-Cu-SSZ-13@MAS catalyst exhibited better hydrothermal stability, with NO_x conversions higher than 80% from 250 to 500 °C. How-

ever, excellent N₂ selectivity could be obtained for all of the aged catalysts, with values > 90% across the entire temperature range. Overall, construction of a core-shell structure is an optimal method to develop zeolite-based catalysts with both excellent NH₃-SCR performance and high hydrothermal stability.

In order to evaluate the degradation in catalyst structure caused by the hydrothermal treatment, XRD measurements were performed for the fresh and aged catalysts. As shown in Fig. S4, the XRD patterns of the catalysts before hydrothermal aging exhibited similar characteristics as their corresponding supports, indicating that microporous or/and mesoporous structures were retained after ion-exchange of the active Cu species. After hydrothermal treatment, the peak intensity of the Cu-SSZ-13 catalyst decreased to some extent, indicating that its crystal structure was partially destroyed. Similarly, all diffraction peaks of the meso-Cu-SSZ-13 catalyst disappeared after hydrothermal treatment, indicating that the crystal structure of the meso-Cu-SSZ-13 catalyst had collapsed. In contrast, there was little change in the diffraction pattern for the meso-Cu-SSZ-13@MAS catalyst, suggesting that the structure of this catalyst remained largely intact during hydrothermal aging. Additionally, no formation of CuO over all the fresh and aged catalysts was evident in the XRD data.

The N₂ adsorption-desorption isotherms of the catalysts before and after hydrothermal aging are shown in Fig. S5a. The fresh catalysts showed isotherms similar to those of their corresponding supports. The textural and structural properties of the catalysts before and after hydrothermal aging are shown in Table 1. Compared with the supports, the S_{BET}, S_{ext}, and V_t were smaller for the corresponding catalysts before hydrothermal aging, due to pore blockage by the active metal phases in the ion-exchange process. However, after hydrothermal treatment, only the S_{BET}, S_{ext}, and V_t of meso-Cu-SSZ-13 were greatly reduced, indicating that its crystal structure had collapsed. This is consistent with the XRD results. Moreover, the pore size distributions of all catalysts were also similar to their corresponding supports (Fig. S5b).

The SEM images of all catalysts before and after hydrothermal aging are shown in Fig. S6. Fresh catalysts and their corresponding supports showed very similar appearances. It is observed that the crystallinity and morphology of the meso-Cu-SSZ-13 sample were severely damaged after hydrothermal treatment at 750 °C for 16 h. For Cu-SSZ-13 sample, some surface defects and fragmentation were observed. In comparison, the morphology of meso-Cu-SSZ-13@MAS remained almost intact. The above observations further confirm that meso-Cu-SSZ-13@MAS has excellent hydrothermal stability.

H₂-TPR experiments were carried out to investigate the effect of hydrothermal aging on the reducibility of Cu species. As shown in Fig. 6, the fresh catalysts showed three reduction peaks (labeled α , γ and β) below 500 °C, indicating that three different types of Cu species are present in these catalysts. According to the literature, the lower temperature reduction peak α may be assigned to the reduction of isolated Cu²⁺ ions in the CHA cage [36]. The middle temperature reduction peak γ corresponds to the reduction of CuO to Cu⁰⁰ [4]. The higher temperature reduction peak β can be attributed to the reduction of Cu²⁺ ions on D6R [36]. In addition, the H₂ consumption peaks above 500 °C were assigned to the reduction of Cu⁺ to Cu⁰⁰, where Cu⁺ is formed from the reduction of isolated Cu²⁺ ions. To make H₂ consumption profiles below 500 °C more accurate, peak fitting process was carried out based on the Gaussian deconvolution. As shown in Fig. S7 and Table 2, it is clearly observed that more CuO species were observed in fresh Cu-SSZ-13 compared to those in the other two fresh samples. Furthermore, most Cu species in meso-Cu-SSZ-13 and meso-Cu-SSZ-13@MAS were Cu²⁺ ions on the D6R. These results indicate that the introduction of mesoporous structure is conducive to Cu species into the ion-exchange sites of SSZ-13 molecular sieve. After

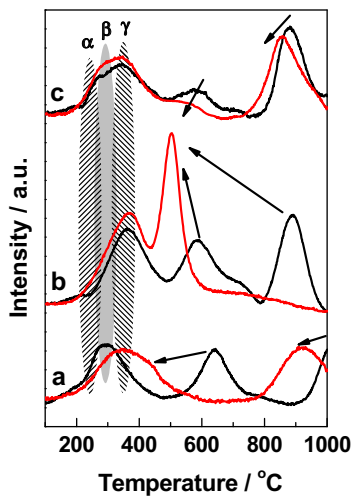


Fig. 6. H_2 -TPR profiles of the Cu-SSZ-13 (a), meso-Cu-SSZ-13 (b) and meso-Cu-SSZ-13@MAS (c) catalysts before and after hydrothermal aging.

Table 2

Quantitative analysis of the H_2 -TPR profiles of the fresh catalysts.

| Samples | peak α ($\mu\text{mol/g}$) | peak β ($\mu\text{mol/g}$) | peak γ ($\mu\text{mol/g}$) |
|--------------------|-------------------------------------|------------------------------------|-------------------------------------|
| Cu-SSZ-13 | 25.5 | 45.1 | 56.6 |
| meso-Cu-SSZ-13 | 1.9 | 6.8 | 126.9 |
| meso-Cu-SSZ-13@MAS | 9.4 | 8.8 | 102.2 |

hydrothermal aging at 750°C , there were some differences in the H_2 -TPR patterns. Among them, the smallest changes were observed for the meso-Cu-SSZ-13@MAS sample. Further, it was found that the reduction peak of Cu^+ to Cu^{00} moved toward a lower temperature, probably due to the weakened interaction between the Cu^+ ion and SSZ-13 as a result of the partial destruction of zeolite structure [37].

EPR experiments were carried out to identify the coordination environment of Cu^{2+} ions on the surface of Cu-SSZ-13, meso-Cu-SSZ-13 and meso-Cu-SSZ-13@MAS catalysts before and after hydrothermal aging. As shown in Fig. 7, there were two major Cu^{2+} species (also labeled α and β) in the three fresh samples, which are assigned to Cu^{2+} ions in the CHA cage ($g_{\parallel} = 2.343$ and $A_{\parallel} = 148.8 \text{ G}$) and on D6R ($g_{\parallel} = 2.371$ and $A_{\parallel} = 135.5 \text{ G}$) [23]. After hydrothermal aging, for Cu-SSZ-13, meso-Cu-SSZ-13, the content of α and β species decreased, and the new Cu^{2+} species (also labeled γ) appeared, which are attributed Cu^{2+} on Al_2O_3 ($g_{\parallel} = 2.316$ and $A_{\parallel} = 154.3 \text{ G}$) [23]. This indicates the collapse of zeolite structure for these two samples [23]. In contrast, both α and β species on meso-Cu-SSZ-13@MAS had a little change and almost no γ species were formed, which suggests the high hydrothermal stability of meso-Cu-SSZ-13@MAS.

NH_3 -TPD experiments were carried out to investigate the evolution of acidity during the process of hydrothermal aging. As shown in Fig. 8, three peaks (labeled η , δ and ϕ) were observed in the fresh samples. Based on analysis in previous studies [22,38,39], the low-temperature peak η was assigned to weakly adsorbed NH_3 , such as physisorbed NH_3 and NH_3 adsorbed on weak Lewis acid sites. The middle desorption peak δ at approximately 300°C is related to NH_3 adsorbed on strong Lewis acidsites, which are created by the exchanged Cu^{2+} ions. The high-temperature peak ϕ at above 400°C was assigned to NH_3 adsorbed on Brønsted acid sites. Further, each NH_3 -TPD curve was deconvoluted by the Gauss curve-fitting method into three separated peaks (Fig. S8). The amounts of different acid sites were calculated, as summarized in Fig. S9. The total acid quantity of meso-Cu-SSZ-13 (1.50 mmol g^{-1}) is obviously larger than that of Cu-SSZ-13 (1.14 mmol g^{-1}), because

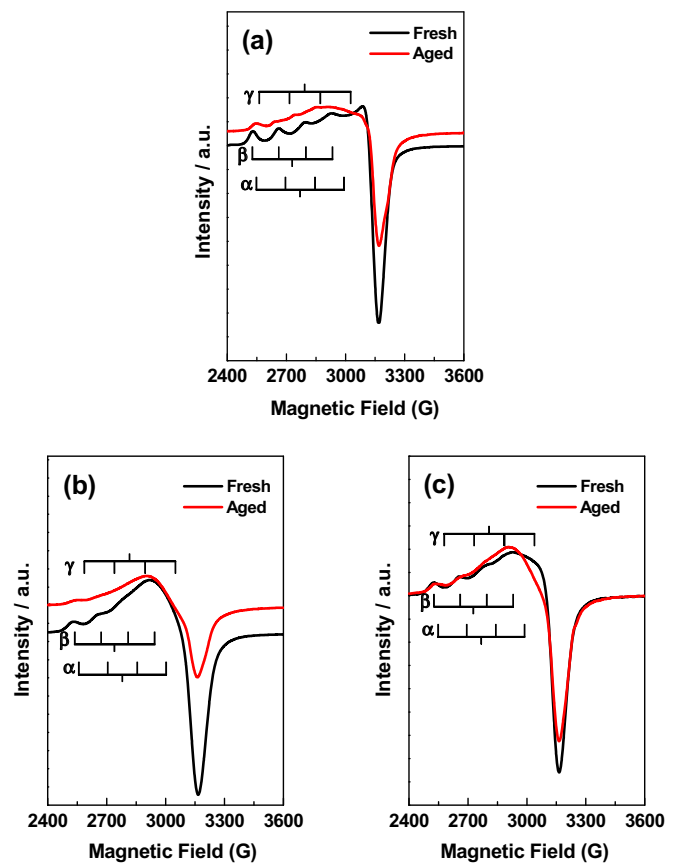


Fig. 7. EPR spectra of Cu-SSZ-13 (a), meso-Cu-SSZ-13 (b) and meso-Cu-SSZ-13@MAS (c) catalysts before and after hydrothermal aging.

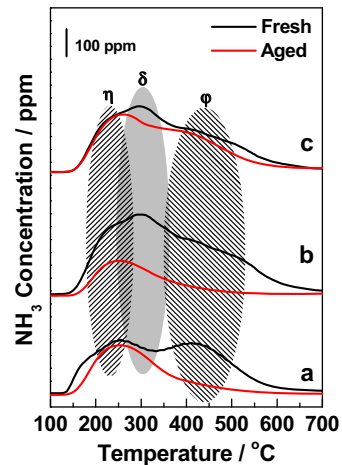


Fig. 8. NH_3 -TPD curves of the Cu-SSZ-13 (a), meso-Cu-SSZ-13 (b) and meso-Cu-SSZ-13@MAS (c) catalysts before and after hydrothermal aging.

the Si/Al ratio was decreased by desilication (Table 1) and the total concentration of Al increased significantly. The total acid quantity of meso-Cu-SSZ-13@MAS was found to be approximately 1.12 mmol g^{-1} , corresponding to approximately 74.7% of that of meso-Cu-SSZ-13 and 98.2% of that of Cu-SSZ-13. Additionally, at similar Cu loadings, the amounts of Lewis acid sites (peak δ) for both meso-Cu-SSZ-13 and meso-Cu-SSZ-13@MAS were larger than those of Cu-SSZ-13, indicating that the more abundant isolated Cu^{2+} ions exist in two former samples. This result suggests that the introduction of a mesoporous structure is conducive to placing more Cu^{2+} species into the ion-exchange sites of SSZ-13. After hydrothermal

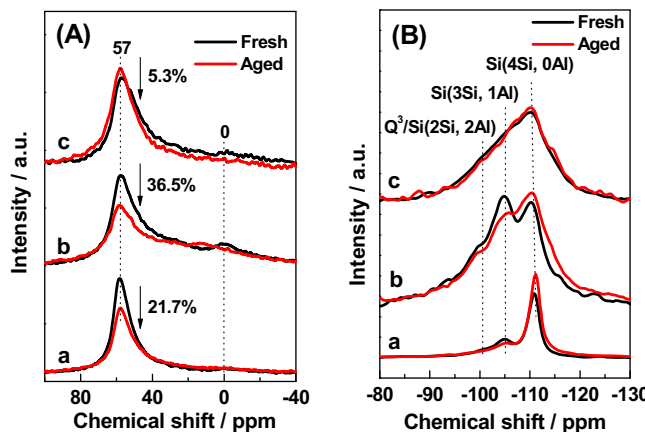


Fig. 9. Solid state ^{27}Al (A) and ^{29}Si NMR (B) spectra of the Cu-SSZ-13 (a), meso-Cu-SSZ-13 (b) and meso-Cu-SSZ-13@MAS (c) catalysts before and after hydrothermal aging.

aging, all the NH_3 desorption peaks over Cu-SSZ-13 and meso-Cu-SSZ-13 samples were reduced, indicating that both the Lewis acid sites and Brønsted acid sites were lost during the hydrothermal process. In comparison, the influence of hydrothermal aging on the acid amount of meso-Cu-SSZ-13@MAS was comparatively smaller.

Solid state NMR experiments were carried out to monitor the differences in the framework of zeolite catalysts before and after hydrothermal aging. ^{27}Al solid state NMR spectra can detect the coordination state of Al species in zeolites. For SSZ-13 zeolite, the feature at 57 ppm is attributed to the framework, tetrahedral Al (Al_f), while the feature at 0 ppm is assigned to the extra-framework octahedral Al [39]. As shown in Fig. 9A, in the fresh samples, a small amount of extra-framework Al atoms were detected in meso-Cu-SSZ-13, while almost all Al atoms stayed as Al_f in Cu-SSZ-13. This finding suggests that dealumination occurred during alkali treatment. However, the extra-framework Al backed into Al_f during the self-assembly process of MAS on the surface of meso-SSZ-13, implying that the Si-OH-Al bond is probably formed at the interface of MAS and meso-SSZ-13 in the meso-Cu-SSZ-13@MAS sample. Furthermore, compared with Cu-SSZ-13, the spectrum width of meso-Cu-SSZ-13 was slight enlarged, indicating that desilication results in non-uniform distribution in the framework Al atoms to some degree. After hydrothermal aging, the intensity of the peak at 57 ppm was reduced significantly on both Cu-SSZ-13 and meso-Cu-SSZ-13. Moreover, compared with Cu-SSZ-13 (decrease by 21.7%), meso-Cu-SSZ-13 (decrease by 36.5%) showed more obvious Al_f loss during hydrothermal treatment. In contrast, the peak intensity on meso-Cu-SSZ-13@MAS (decrease by 5.3%) has little change. The observed hydrothermal stability of the catalysts is consistent with the change in their SCR activity. Note that no obvious increase of extra-framework Al was observed on the aged catalyst. This finding may be observed because the extra-framework Al atoms, generated during hydrothermal treatment, interact strongly with the paramagnetic Cu ions to form CuAlO_x species [5].

Fig. 9B presents the ^{29}Si MAS NMR spectra obtained from the Cu-SSZ-13, meso-Cu-SSZ-13 and meso-Cu-SSZ-13@MAS catalysts before and after hydrothermal aging. For the fresh Cu-SSZ-13 sample, features at -110 and -105 ppm were attributed to Si(4Si, 0Al) and Si(3Si, 1Al), respectively [40]. For the fresh meso-Cu-SSZ-13 sample, tetrahedral Si in Si(4Si, 0Al) and Si(3Si, 1Al) was also observed at -110 and -105 ppm, where the latter become dominant. Note that a new feature at -101 ppm was observed on this sample. This consists of overlapping peaks from Si(2Si, 2Al) and Si atoms with terminal hydroxyl groups at the defect sites Si(SiO₃OH) (Q³), [41]. For the fresh meso-Cu-SSZ-13@MAS sample, feature at

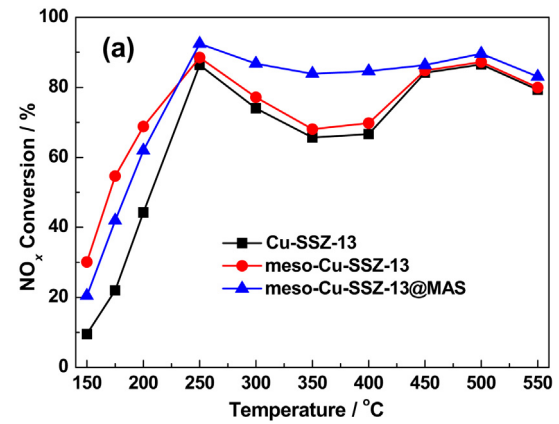


Fig. 10. NO_x conversion with C_3H_6 as a function of temperature in the NH_3 -SCR reaction over the catalysts. NH_3 -SCR with C_3H_6 reaction conditions: $[\text{NO}] = [\text{NH}_3] = [\text{C}_3\text{H}_6] = 500 \text{ ppm}$, $[\text{O}_2] = 5\%$, $[\text{H}_2\text{O}] = 5\%$, N_2 balance, total flow rate 200 mL min^{-1} and $\text{GHSV} = 400,000 \text{ h}^{-1}$.

Table 3

TGA coke deposits over the catalysts.

| Samples | Amount of coke ^a (wt%) |
|--------------------|-----------------------------------|
| Cu-SSZ-13 | 3.77 |
| meso-Cu-SSZ-13 | 5.29 |
| meso-Cu-SSZ-13@MAS | 1.81 |

^a Amount of coke: 3 h on stream with 500 ppm C_3H_6 at 350 °C.

-110 ppm assigned to Si(4Si, 0Al) became dominant again. After hydrothermal treatment, the amount of Si(4Si, 0Al) increased on both Cu-SSZ-13 and meso-Cu-SSZ-13, implying that obvious dealumination occur on these two catalysts. Based on XRD, and ^{29}Si , ^{27}Al solid state NMR results, it seems that dealumination and collapse of the structure occur simultaneously on meso-Cu-SSZ-13. In contrast, the amount of Si(4Si, 0Al) on meso-Cu-SSZ-13@MAS showed little change, further demonstrating its high hydrothermal stability.

3.4. Propene poisoning resistance

In order to study the effect of propene on the catalytic activities, NO_x conversions were measured with C_3H_6 over the catalysts, and these results are shown in Fig. 10. After C_3H_6 was included into the feed gas, the catalytic activities were inhibited across the entire temperature range, particularly in the region of 300–400 °C. At the low temperatures (≤ 250 °C), the decrease in NO_x conversion is probably due to the adsorption of NH_3 onto the catalyst surface by the competitive adsorption of C_3H_6 . In the medium temperature region (300–400 °C), the catalytic performances decreased sharply. The corresponding results of C_3H_6 oxidation reaction indicate that the oxidation of C_3H_6 increases quickly from 300 °C (Fig. S10). Note that it was particularly difficult to obtain steady-state performance in the temperature region of 300–400 °C because NO_x conversions continued to decrease with extended C_3H_6 exposure, even after 3 h, indicating that some poisons were accumulating on the catalyst surface. Previous studies have demonstrated that in the presence of C_3H_6 , a certain amount of coke is formed over the Cu-SSZ-13 catalyst during NH_3 -SCR process [24,25]. Thus, coke formation may be responsible for the deactivation of catalysts in this temperature region. Additionally, the amount of coke on the catalysts was estimated from weight loss profiles of TGA. As shown in Table 3, the amount of coke formation on meso-Cu-SSZ-13@MAS was found to be less compared with that on Cu-SSZ-13 and meso-Cu-SSZ-13. However, the NO_x conversions started to markedly increase again in the high temperature region above 400 °C. This phenomenon can be explained as follows: (1) at high temperatures (> 400 °C),

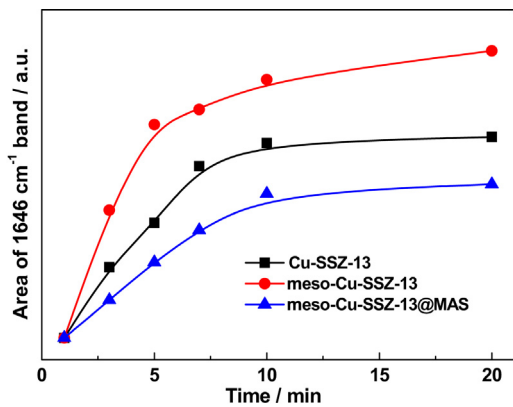


Fig. 11. Formation of acrolein species (indicated by band area at 1646 cm^{-1}) at 200°C upon passing $500\text{ ppm NO} + 5\%\text{ O}_2 + 500\text{ ppm C}_3\text{H}_6/\text{N}_2$ over the fresh catalysts.

most of the coke depositions can be quickly removed in an oxygen-rich environment; (2) another reaction such as HC-SCR may occur during the NH_3 -SCR reaction with C_3H_6 [25]. Overall, the influence of propene on the catalytic activities is not pronounced over *meso*-Cu-SSZ-13@MAS compared to that over Cu-SSZ-13 and *meso*-Cu-SSZ-13.

In-situ DRIFTS experiments were conducted and IR spectra were recorded with the introduction of various gases into the cell at 200°C for 30 min. Fig. S11a shows the IR spectra for chemical species adsorbed onto the surface of the Cu-SSZ-13 sample after a flow of various feed gases. Two bands at 1615 and 1452 cm^{-1} , assigned to Lewis acid-bound NH_3 and protonated NH_3 , respectively, are observed in a NH_3 only feed [15,42]. Additionally, three bands in the range of 3100 – 3400 cm^{-1} were assigned to N–H stretching vibrations [42]. Meanwhile, the bands in the range of 3500 – 3800 cm^{-1} represent the consumption of surface hydroxyl [16]. When C_3H_6 was simultaneously included in the feed gases with NH_3 , a similar spectrum to that with only NH_3 present was obtained. However, the intensity of the band decreased to some extent, probably due to the competitive adsorption of C_3H_6 . Furthermore, no C_3H_6 -related adsorption peaks were observed, indicating that strong NH_3 adsorption would take place easily, even in the presence of C_3H_6 . In addition, the bands for the *meso*-Cu-SSZ-13 and *meso*-Cu-SSZ-13@MAS catalysts (Fig. S11b and c), assigned to different compounds on the surfaces of these two catalysts, are similar to those over Cu-SSZ-13 in the presence of the same feed gases.

To demonstrate the effect of propene on NO_x adsorption, DRIFTS spectra were recorded as a function of time after $500\text{ ppm C}_3\text{H}_6 + 500\text{ ppm NO} + 5\%\text{ O}_2/\text{N}_2$ was introduced into the sample cell at 200°C (Fig. S12). Each DRIFTS spectrum was deconvoluted by the Gauss curve fitting method. The results show that the species mainly adsorbed on these catalysts are hydrocarbons (at 1587 cm^{-1}), nitrate species (at 1573 , 1597 and 1625 cm^{-1}) and acrolein species (at 1646 cm^{-1}) [16,25,43,44]. Moreover, after $\text{NO} + \text{O}_2 + \text{C}_3\text{H}_6/\text{N}_2$ was introduced, the catalyst surface was gradually dominated by the adsorbed acrolein species. On the basis of our DRIFTS results and prior research [45], the formation mechanism of acrolein species is shown in Fig. S13. The formed acrolein species is primarily adsorbed on Cu-sites, which blocks the adsorption of NO_x . This is because the adsorbed NO_x species are also inclined to be adsorbed on Cu-sites (Fig. S14). In addition, Fig. 11 summarizes the results of the formation of acrolein species (indicated by band area at 1646 cm^{-1}) at 200°C . For Cu-SSZ-13, the intensity of the IR band corresponding to acrolein species increased and became stable until 15 min. In contrast, the increasing trend of this IR band for

meso-Cu-SSZ-13@MAS was obviously lower when the same feed gases were introduced. However, acrolein peak intensity continued to increase over the *meso*-Cu-SSZ-13 catalyst, and the content of the adsorbed acrolein species on its surface was significantly higher than on the other two catalysts after 20 min. In summary, fewer acrolein species form on *meso*-Cu-SSZ-13@MAS compared with Cu-SSZ-13 and *meso*-Cu-SSZ-13.

4. Discussion

4.1. Effect of mesoporous structure on NH_3 -SCR activity

The *meso*-Cu-SSZ-13 and *meso*-Cu-SSZ-13@MAS catalysts exhibited high SCR activity than the Cu-SSZ-13 catalyst across the entire temperature range. This activity difference can be attributed to the introduction of the mesoporous structure into SSZ-13 molecular sieve.

Many studies have demonstrated that the isolated Cu^{2+} ions are the active sites for NH_3 -SCR reaction on the Cu-SSZ-13 catalyst [11,13,14]. The H_2 -TPR and NH_3 -TPD results demonstrate that isolated Cu^{2+} are more abundant in both *meso*-Cu-SSZ-13 and *meso*-Cu-SSZ-13@MAS catalysts compared with the Cu-SSZ-13 catalyst. For the Cu-SSZ-13 catalyst, the small pore openings of the SSZ-13 zeolite allow Cu ion-exchange to occur only in the outer parts of its crystal [46]. Furthermore, a part of the ion-exchanged Cu species would migrate and transform during the thermal treatment process, and aggregate into some CuO species on the external surface of SSZ-13. The above situation can be improved when a mesoporous structure is introduced into the crystals of SSZ-13 (Fig. S15). This is because external surface area increases accordingly (Table 1). Moreover, more ion-exchange sites in the internal parts of the SSZ-13 crystal can be exposed by the introduction of mesoporous structures. More Cu species can then enter into the ion-exchange sites easily and smoothly. Finally, the SCR activity of the Cu-SSZ-13 catalyst is enhanced because of the availability of more accessible active Cu site. Further, at high temperatures ($\geq 400^\circ\text{C}$), NO_x conversions start to drop due to the non-selective NH_3 oxidation reaction. The existence of CuO_x on the zeolite catalyst aggravates this situation [15]. The H_2 -TPR results show that more CuO species are observed in Cu-SSZ-13 in comparison with *meso*-Cu-SSZ-13 and *meso*-Cu-SSZ-13@MAS. Thus, the relatively poor SCR activity above 400°C for Cu-SSZ-13 shown in Fig. 5 is most likely caused by non-selective NH_3 oxidation, catalyzed by CuO species [4,8,19,47].

In addition, intra-crystalline (pore) diffusion limitations, which are inherited from the microporous nature of the zeolite structures, can substantially restrict the catalytic performance of zeolite-based catalysts. For SSZ-13, these diffusion limitations are more serious owing to its small pore openings ($\sim 3.8\text{ \AA}$). However, when a mesoporous structure is introduced, the diffusion path length inside the SSZ-13 zeolite becomes shorter and the diffusion resistance can be reduced remarkably. The kinetics results show that *meso*-Cu-SSZ-13 and *meso*-Cu-SSZ-13@MAS display higher E_a value than that of Cu-SSZ-13, indicating the fewer pore diffusion limitations exist in the former two [35]. Furthermore, it is interesting to note that the *meso*-Cu-SSZ-13 sample has the highest E_a value. Although *meso*-Cu-SSZ-13@MAS has the highest surface area and pore volume among the three samples, it shows a relatively low E_a of 63 kJ/mol , suggesting that more pore diffusion limitations exist in *meso*-Cu-SSZ-13@MAS. This difference can be explained as follows. According to the catalyst characterization above, the increase in surface area and pore volume for *meso*-SSZ-13@MAS in comparison with *meso*-SSZ-13 is due to the introduction of the MAS shell onto *meso*-SSZ-13. However, there are very few ion-exchange sites (Al sites) in the MAS shell (Table 1) and most ion-exchange sites of *meso*-SSZ-13@MAS are mainly from the *meso*-SSZ-13 core. Fur-

ther, the results of ^{27}Al solid state NMR show that Si-OH-Al bonds are formed at the interface of MAS and *meso*-SSZ-13. Therefore, ion-exchange sites on the external surface of the *meso*-SSZ-13 core are covered by the MAS shell, and the main ion-exchange sites are in the internal parts of SSZ-13 crystal. Finally, the most active Cu species only exist in the internal parts of the SSZ-13 crystal and this increases the pore diffusion limitations.

4.2. Effect of core-shell structure on hydrothermal stability

Hydrothermal treatment can influence the physicochemical properties and reactant adsorption abilities of zeolite catalysts [21]. Although Cu-SSZ-13 has better hydrothermal stability in comparison with other Cu-zeolite catalysts (such as Cu-ZSM-5, Cu-Y, and Cu-beta) [5], prolonged hydrothermal treatment can still result in significantly reduced SCR performance. The decrease in SCR performance is due to the destruction of zeolite structure and/or agglomeration of Cu [48]. Our previous study has demonstrated that dealumination first occurs in Cu-SSZ-13, after which the detached $\text{Al}(\text{OH})_3$ species deactivate the Cu species [49]. Additionally, Fickel et al. comparatively studied the hydrothermal stability of Cu-exchanged small-pore (Cu-SSZ-13, Cu-SAPO-34, etc.) and medium-pore (Cu-ZSM-5) zeolite catalysts [50]. They found that the detached $\text{Al}(\text{OH})_3$ species cannot enter or exit the pores of the CHA structure because the kinetic diameter of $\text{Al}(\text{OH})_3$ (5.03 Å) is larger than the largest pore window (3.8 Å \times 3.8 Å) in the CHA structure. The detached $\text{Al}(\text{OH})_3$ species would reattach to the CHA framework when the catalyst was subsequently cooled and maintain the integrity of the structure. Therefore, it can be speculated that dealumination occurring on the surface of the SSZ-13 crystal primarily accounts for zeolite structure destruction during hydrothermal treatment. Meanwhile, certain active Cu species may migrate out of the ion-exchange sites of the SSZ-13 framework structure during hydrothermal treatment. Finally, the detached $\text{Al}(\text{OH})_3$ species could migrate on the catalyst surface and interact with Cu species onto form CuAlO_x species [5,51].

The XRD and SEM results show that the partial crystal structures of Cu-SSZ-13 are destroyed during hydrothermal aging. Meanwhile, the crystallinity and morphology of the *meso*-Cu-SSZ-13 sample are severely damaged. In comparison, the crystal structures of *meso*-Cu-SSZ-13@MAS remain almost intact. However, the morphology difference between *meso*-Cu-SSZ-13 and *meso*-Cu-SSZ-13@MAS is only that the latter has a MAS shell. Therefore, the high hydrothermal stability of *meso*-Cu-SSZ-13@MAS must be related to the MAS shell. XRD results shown in Fig. 2b suggest that MAS still exhibits characteristic diffraction peaks due to the CHA topology, although they are weak in intensity. Furthermore, the FT-IR spectrum of MAS shows four bands at 468, 534, 646, and 800 cm^{-1} (Fig. S16). The bands at 468 cm^{-1} and 634 cm^{-1} express the vibration of TO_4 units, and the band at 646 cm^{-1} is attributed to the vibration of double six-membered oxygen rings [52]. The symmetric T-O-T vibration is observed at 800 cm^{-1} . Overall, XRD and FT-IR characterizations demonstrate the existence of CHA-structured components in MAS. Because *meso*-SSZ-13@MAS is self-assembled using the same preparation procedures as MAS in the presence of *meso*-SSZ-13 crystals, its MAS shell therefore contains the CHA-type aluminosilicate species, which serve as the “crushed stone”. From the additional evidence of TEM, it is proposed that the MAS shell has a “concrete with crushed stone”-like mesostructure. At the atomic level, the leached silica and alumina species constitute a worm-like framework as the “concrete”. This structural feature of the MAS shell can make it resistant to severe hydrothermal treatment. For *meso*-Cu-SSZ-13@MAS, the *meso*-Cu-SSZ-13 core is enclosed by the MAS shell (Fig. 4d₂ and S1) and Si-OH-Al bonds are formed at the interface of MAS and *meso*-SSZ-13 (Fig. 9A). There-

fore, the MAS shell can effectively prevent dealumination on the surface of the *meso*-SSZ-13 core during hydrothermal aging, which is verified by ^{27}Al NMR. Finally, the hydrothermal stability of the *meso*-Cu-SSZ-13@MAS catalyst is enhanced distinctly.

4.3. Effect of core-shell structure on propene poisoning resistance

In our previous results [25,53], the decrease of the DeNO_x catalytic performance over zeolite catalysts in the presence of propene was primarily attributed to the coke depositions on the active species. Coke depositions can also decrease the surface area and pore volume of the zeolite catalysts. However, there are some fundamental differences in the pore geometries of these zeolite catalysts, and the catalysts' resistance to hydrocarbon poisoning depends on pore geometry. For instance, ZSM-5 with relatively large channels favors effective diffusion of propene, and coke depositions can form on its pores and external surface [24]. In contrast, the pore openings of SSZ-13 (~3.8 Å) are smaller than the kinetic diameter of a propene molecule (~4.5 Å) [24], which inhibits the propene molecule from directly entering the pores of SSZ-13. The propene oxidation reaction leading to polymerization can only occur on the external surface of SSZ-13, resulting in coke depositions. Moreover, the extent of coke depositions is related to the acidity amount of zeolite catalysts because hydrocarbons are most active on the acid sites [53,54]. As shown in Fig. S9, after the introduction of the MAS shell onto *meso*-Cu-SSZ-13, the acidity amount of *meso*-Cu-SSZ-13@MAS is less than that of *meso*-Cu-SSZ-13. Obviously, this loss results from the decrease of acid sites on the *meso*-Cu-SSZ-13 surface. In addition, although *meso*-Cu-SSZ-13@MAS and Cu-SSZ-13 have a similar acidity amount, most acid sites of *meso*-Cu-SSZ-13@MAS are in its pores because its external surface is covered by the MAS shell. Therefore, *meso*-Cu-SSZ-13@MAS shows higher propene poisoning resistance due to fewer active sites for the propene oxidation reaction. This finding can be demonstrated by the in-situ DRIFTS results. Compared with Cu-SSZ-13 and *meso*-Cu-SSZ-13, fewer acrolein species are formed on *meso*-Cu-SSZ-13@MAS.

5. Conclusions

A core-shell structured *meso*-SSZ-13@MAS material was synthesized by combining desilication using alkaline solution with subsequent self-assembly using a triblock copolymer (P123). Next, the corresponding catalyst was prepared by a copper ion-exchange method. The *meso*-SSZ-13@MAS catalyst can simultaneously solve three major problems, i.e., low temperature activity, hydrothermal stability and propene poisoning resistance, existing in the previous Cu-SSZ-13 catalyst for NO_x emission control from diesel engine exhaust.

When a mesoporous structure is introduced into SSZ-13 molecular sieve, more active Cu species can enter the ion-exchange sites easily and smoothly. Additionally, the pore diffusion limitations are reduced due to the reduction in diffusion path length inside the SSZ-13 zeolite. Therefore, the SCR activity of the *meso*-SSZ-13@MAS catalyst is enhanced across the entire temperature range. The XRD, FT-IR and TEM results indicate that the MAS shell has a “concrete with crushed stone”-like mesostructure. The ^{27}Al NMR results show that this MAS shell could prevent the dealumination of the *meso*-SSZ-13 core effectively and thus improve the hydrothermal stability of the *meso*-Cu-SSZ-13@MAS catalyst. Finally, the NH_3 -TPD and in-situ DRIFTS results suggest that *meso*-Cu-SSZ-13@MAS possesses higher hydrocarbon poisoning resistance because it has fewer active sites for propene oxidation reaction.

Acknowledgements

This work was financially supported by the National Natural Science Fund of China (Grant Nos. 21325731, 51478241 and 21221004) and the National High-Tech Research and Development (863) Program of China (Grant No. 2013AA065401, 2013AA065304). The authors would also like to acknowledge China Postdoctoral Science Foundation (043206011).

Appendix A. Supplementary data

Supplementary data associated with this article can be found, in the online version, at <http://dx.doi.org/10.1016/j.apcatb.2016.04.058>.

References

- [1] S. Brandenberger, O. Kröcher, A. Tissler, R. Althoff, *Catal. Rev.* 50 (2008) 492.
- [2] J.H. Kwak, R.G. Tonkyn, D.H. Kim, J. Szanyi, C.H.F. Peden, *J. Catal.* 275 (2010) 187.
- [3] L. Wang, W. Li, G. Qi, D. Weng, *J. Catal.* 289 (2012) 21.
- [4] J. Xue, X. Wang, G. Qi, J. Wang, M. Shen, W. Li, *J. Catal.* 297 (2013) 56.
- [5] J.H. Kwak, D. Tran, S.D. Burton, J. Szanyi, J.H. Lee, C.H.F. Peden, *J. Catal.* 287 (2012) 203.
- [6] S.I. Zones, US Patent 4 544 538, 1985.
- [7] B. Chen, R. Xu, R. Zhang, N. Liu, *Environ. Sci. Technol.* 48 (2014) 13909.
- [8] L. Xie, F. Liu, L. Ren, X. Shi, F.-S. Xiao, H. He, *Environ. Sci. Technol.* 48 (2014) 566.
- [9] R. Martínez-Franco, M. Moliner, J.R. Thøgersen, A. Corma, *ChemCatChem* 5 (2013) 3316.
- [10] J.H. Kwak, H.Y. Zhu, J.H. Lee, C.H.F. Peden, J. Szanyi, *Chem. Commun.* 48 (2012) 4758.
- [11] U. Deka, A. Juhin, E.A. Eilertsen, H. Emerich, M.A. Green, S.T. Korhonen, B.M. Weckhuysen, A.M. Beale, *J. Phys. Chem. C* 116 (2012) 4809.
- [12] S.A. Bates, A.A. Verma, C. Paolucci, A.A. Parekh, T. Anggara, A. Yezerets, W.F. Schneider, J.T. Miller, W.N. Delgass, F.H. Ribeiro, *J. Catal.* 312 (2014) 87.
- [13] D.W. Fickel, J.M. Fedeyko, R.F. Lobo, *J. Phys. Chem. C* 114 (2010) 1633.
- [14] S.T. Korhonen, D.W. Fickel, R.F. Lobo, B.M. Weckhuysen, A.M. Beale, *Chem. Commun.* 47 (2011) 800.
- [15] L. Ma, Y. Cheng, G. Cavataio, R.W. McCabe, L. Fu, J. Li, *Appl. Catal. B* 156–157 (2014) 428.
- [16] D. Wang, L. Zhang, K. Kamasamudram, W.S. Epling, *ACS Catal.* 3 (2013) 871.
- [17] H. Zhu, J.H. Kwak, C.H.F. Peden, J. Szanyi, *Catal. Today* 205 (2013) 16.
- [18] J.H. Kwak, J.H. Lee, S.D. Burton, A.S. Lipton, C.H.F. Peden, J. Szanyi, *Angew. Chem. Int. Ed.* 52 (2013) 9985.
- [19] F. Gao, E.D. Walter, E.M. Karp, J. Luo, R.G. Tonkyn, J.H. Kwak, J. Szanyi, C.H.F. Peden, *J. Catal.* 300 (2013) 20.
- [20] F. Gao, E.D. Walter, M. Kollar, Y.L. Wang, J. Szanyi, C.H.F. Peden, *J. Catal.* 319 (2014) 1.
- [21] L. Ma, Y. Cheng, G. Cavataio, R.W. McCabe, L. Fu, J. Li, *Chem. Eng. J.* 225 (2013) 323.
- [22] D. Wang, Y. Jangjou, Y. Liu, M.K. Sharma, J. Luo, J. Li, K. Kamasamudram, W.S. Epling, *Appl. Catal. B* 165 (2015) 438.
- [23] Y.J. Kim, J.K. Lee, K.M. Min, S.B. Hong, I.-S. Nam, B.K. Cho, *J. Catal.* 311 (2014) 447.
- [24] Q. Ye, L. Wang, R.T. Yang, *Appl. Catal. A* 427–428 (2012) 24.
- [25] L. Ma, W. Su, Z. Li, J. Li, L. Fu, J. Hao, *Catal. Today* 245 (2015) 16.
- [26] F. Gao, Y. Wang, N.M. Washton, M. Kollar, J. Szanyi, C.H.F. Peden, *ACS Catal.* 5 (2015) 6780.
- [27] L. Olsson, K. Wijayanti, K. Leistner, A. Kumar, S.Y. Joshi, K. Kamasamudram, N.W. Currier, A. Yezerets, *Appl. Catal. B* 183 (2016) 394.
- [28] J. Kwak, D. Tran, J. Szanyi, C.H.F. Peden, J. Lee, *Catal. Lett.* 142 (2012) 295.
- [29] M. Zammit, C.L. DiMaggio, C.H. Kim, C.K. Lambert, G.G. Muntean, C.H.F. Peden, J.E. Park, K. Howden, Future Automotive Aftertreatment Solutions: The 150 °C Challenge Workshop Report, US Drive Report, Southfield, MI, 2013, p. 7.
- [30] J.H. Lee, M.J. Paratore, D.B. Brown, *SAE Int. J. Fuels Lubr.* 1 (2009) 96.
- [31] D. Zhao, J. Feng, Q. Huo, N. Melosh, G.H. Fredrickson, B.F. Chmelkaand, G.D. Stucky, *Science* 279 (1998) 548.
- [32] M.J. Treacy, J.B. Higgins, Collection of Simulated XRD Patterns for Zeolites, 5th ed., Elsevier, Amsterdam, 2007, p. 112.
- [33] J.C. Groen, S. Abello, L.A. Villaescusa, J. Perez-Ramirez, *Microporous Mesoporous Mater.* 114 (2008) 93.
- [34] X.F. Li, R. Prins, J.A. van Bokhoven, *J. Catal.* 262 (2009) 257.
- [35] F. Gao, E.D. Walter, N.M. Washton, J. Szanyi, C.H.F. Peden, *ACS Catal.* 3 (2013) 2083.
- [36] J.H. Kwak, H. Zhu, J.H. Lee, C.H.F. Peden, J. Szanyi, *Chem. Commun.* 48 (2012) 4758.
- [37] R. Bulánek, B. Wichterlová, Z. Sobálik, J. Tichý, *Appl. Catal. B* 31 (2001) 135.
- [38] D. Wang, F. Gao, C.H.F. Peden, J. Li, K. Kamasamudram, W.S. Epling, *ChemCatChem* 6 (2014) 1579.
- [39] F. Gao, N.M. Washton, Y. Wang, M. Kollar, J. Szanyi, C.H.F. Peden, *J. Catal.* 331 (2015) 25.
- [40] G. Engelhardt, D. Michel, High-Resolution Solid State NMR of Silicates and Zeolites, Wiley, New York, 1987.
- [41] E.A. Eilertsen, B. Arstad, S. Svelle, K.P. Lillerud, *Microporous Mesoporous Mater.* 153 (2012) 94.
- [42] L. Xie, F. Liu, K. Liu, X. Shi, H. He, *Catal. Sci. Technol.* 4 (2014) 1104.
- [43] M.P. Ruggeri, I. Nova, E. Tronconi, J.A. Pihl, T.J. Toops, W.P. Partridge, *Appl. Catal. B* 166–167 (2015) 181.
- [44] J.Y. Luo, H. Oh, C. Henry, W. Epling, *Appl. Catal. B* 123 (2012) 296.
- [45] R. Raj, M.P. Harold, V. Balakotaiah, *Ind. Eng. Chem. Res.* 52 (2013) 15455.
- [46] P.N.R. Vennestrom, A. Katerinopoulou, R.R. Tiruvalam, A. Kustov, P.G. Moses, P. Concepcion, A. Corma, *ACS Catal.* 3 (2013) 2158.
- [47] F. Gao, E.D. Walter, N.M. Washton, J. Szanyi, C.H.F. Peden, *Appl. Catal. B* 162 (2015) 501.
- [48] S.J. Schmiege, S.H. Oh, C.H. Kim, D.B. Brown, J.H. Lee, C.H.F. Peden, D.H. Kim, *Catal. Today* 184 (2012) 252.
- [49] W. Su, Z. Li, Y. Peng, J. Li, *Phys. Chem. Chem. Phys.* 17 (2015) 29142.
- [50] D.W. Fickel, E. D'Addio, J.A. Lauterbacha, R.F. Lobo, *Appl. Catal. B* 102 (2011) 441.
- [51] M. Richter, M.J.G. Fait, R. Eckelt, M. Schneider, J. Radnik, D. Heidemann, R. Fricke, *J. Catal.* 245 (2007) 11.
- [52] T. Zhang, J. Li, J. Liu, D. Wang, Z. Zhao, J. Li, K. Cheng, *AIChE J.* 61 (2015) 3825.
- [53] L. Ma, J. Li, Y. Cheng, C.K. Lambert, L. Fu, *Environ. Sci. Technol.* 46 (2012) 1747.
- [54] J.-Y. Luo, H. Oh, C. Henry, W. Epling, *Appl. Catal. B* 123–124 (2012) 296.